Applying multi-pass friction stir processing to refine the microstructure and enhance the strength, ductility and corrosion resistance of WE43 magnesium alloy

Eivani, A. R.; Mehdizade, M.; Chabok, S.; Zhou, J.

DOI
10.1016/j.jmrt.2021.03.021

Publication date
2021

Document Version
Final published version

Published in
Journal of Materials Research and Technology

Citation (APA)
Eivani, A. R., Mehdizade, M., Chabok, S., & Zhou, J. (2021). Applying multi-pass friction stir processing to refine the microstructure and enhance the strength, ductility and corrosion resistance of WE43 magnesium alloy. *Journal of Materials Research and Technology*, *12*, 1946-1957. https://doi.org/10.1016/j.jmrt.2021.03.021

JOURNAL OF MATERIALS RESEARCH AND TECHNOLOGY 2021;12:1946–1957

Available online at www.sciencedirect.com

jmr&t

Journal of Materials Research and Technology

journal homepage: www.elsevier.com/locate/jmrt

Original Article

Applying multi-pass friction stir processing to refine the microstructure and enhance the strength, ductility and corrosion resistance of WE43 magnesium alloy

A.R. Eivani [a,*], M. Mehdizade [a], S. Chabok [a], J. Zhou [b]

[a] School of Metallurgy and Materials Engineering, Iran University of Science and Technology, Tehran, Iran
[b] Department of Biomechanical Engineering, Delft University of Technology, Mekelweg 2, Delft, 2628 CD, the Netherlands

ARTICLE INFO

Article history:
Received 4 January 2021
Accepted 3 March 2021
Available online 14 March 2021

Keywords:
Magnesium
Friction stir processing
Microstructure
Mechanical properties
Corrosion

ABSTRACT

Magnesium alloys have many unique properties, mostly benefitting from the low density of magnesium. However, they are not competitive, when compared with other lightweight materials, such as aluminum alloys, particularly in ductility and corrosion resistance. There is a strong need to improve the mechanical properties and corrosion resistance of magnesium alloys. In the present research, friction stir processing (FSP) as a severe plastic deformation process was applied to the WE43 magnesium alloy. The effect of FSP up to 6 passes on the grain structure, second-phase particle distribution, mechanical properties and corrosion resistance of the alloy was investigated. It was found that a continuous network of second-phase particles was present at the grain boundaries, which was considered to be one of the main causes for the poor ductility of the alloy in the as-annealed state. By applying two passes of FSP, the grain structure was significantly refined, changing from an average grain size of 12.4 to 2.5 μm. By further FSP, the grain structure continued to refine to an average grain size of 1.4 μm after 4 passes and remained unchanged after 6 passes. However, the fragmentation and redistribution of second-phase particles continued to occur during the 4th and 6th passes of FSP. Because of these microstructural changes, the uniform strain to maximum stress and the strength of specimens gradually improved with increasing number of FSP passes. The corrosion resistance of the alloy was found to be improved by applying 6 passes of FSP, compared to that of the alloy in the initial as-annealed state, which was attributed to the fragmentation and redistribution of second-phase particles. By applying FSP, the uniformity of the protective passive layer was improved and, in the meantime, the intensity of micro-galvanic coupling leading to pitting corrosion was decreased.

---

* Corresponding author.
E-mail address: aeivani@iust.ac.ir (A.R. Eivani).

https://doi.org/10.1016/j.jmrt.2021.03.021

1. Introduction

Magnesium and its alloys have high specific elastic modulus and strength values, which opens up a wide range of possible applications where weight reduction is important, e.g., in the biomedical [1–3], military [4–7] and transport [8–12] industries. Despite superior strength-to-density ratios [8,13–15], they suffer from poor ductility [8,13–15] and corrosion resistance [16–20], making them less competitive to other light metals, such as aluminum alloys. These weaknesses are inherent to magnesium and related to the microstructures. The poor ductility is, for example, due to the hexagonal close packed (HCP) crystal structure of magnesium with a limited number of slip systems at room temperature and also due to a coarse grain structure, especially in the as-cast condition [21–29]. The poor corrosion resistance of magnesium is attributed to its low electromotive force (EMF), corresponding to a high chemical activity and a small amount of negative electrochemical potential. The poor corrosion resistance is also related to the presence of impurities and second-phase particles, inducing localized corrosion. Understanding the mechanisms and finding way to decrease the corrosion rate of magnesium alloys have been a priority area of research for two decades [16–20]. In addition, although Mg and its alloys have high specific elastic moduli and strengths, further enhancements in strength are strongly desired, as this can result in lighter structural parts [9]. Alloying has been found to be an effective way to improve both mechanical properties, i.e., strength and ductility, and corrosion resistance [14,15]. Improved mechanical properties and corrosion resistance by adding rare earth elements have been reported [30–34].

While the approach to improving mechanical and corrosion properties by alloying is successful, it results in the formation of second-phase particles in the microstructure, which can in turn deteriorate the ductility and corrosion properties of magnesium alloys [16–20,35,36]. The presence of second-phase particles limits the uniform corrosion and enhances localized corrosion, particularly pitting corrosion. The negative effect of second-phase particles can again be attributed to the very low EMF of Mg, which causes the micro-galvanic effect, with second-phase particles acting as the cathode and the α-Mg matrix as the anode.

Another approach, from the perspective of materials processing, including casting and forming, has been also used to improve the mechanical properties and corrosion resistance by reducing grain sizes and second-phase particle sizes [37–45]. Thermomechanical processing, including severe plastic deformation (SPD), has been found to be an effective way to achieve desired microstructural modifications [46–53]. However, the poor deformability of Mg and its alloys limits the application of the thermomechanical approach; precise control over temperature and deformation rate is not easy or even not feasible [54–57]. For example, temperature management during multi-pass rolling requires constant supply of thermal energy. Temperature stability during equal channel angular processing (ECAP) appears to be more easily under control. However, still a large amount of heat loss occurs during ECAP, making it difficult to maintain the whole tooling set-up, including the die, at a desired high temperature. Among the thermomechanical processes, friction stir processing (FSP) offers an easy way to achieve process stability [58]. This is because, during this process, heat is generated by itself, due to the rotation of the processing tool. Only a few process parameters, i.e., rotation and moving speeds, should be controlled to make FSP stay within the defined processing window [58].

FSP has already been used for thermomechanical processing of Mg and its alloys in order to achieve enhanced mechanical properties or improved corrosion resistance [58–67]. A critical analysis of the relevant literature shows that previous research was focused either on deformation, microstructure and mechanical properties or on corrosion resistance. Systematic research is missing. The main objective of the present research was to establish the correlations between FSP pass number, grain structure, second-phase particles sizes and distribution, mechanical properties and corrosion resistance. The WE43 magnesium alloy was used as an experimental material for this research.

2. Experimental details

WE43 magnesium alloy plates with a thickness of 10 mm were received in the hot-rolled condition. The chemical composition of the alloy determined by optical emission spectroscopy (OES) is shown in Table 1. Prior to FSP, the hot rolled sheets have to be annealed to acquire an equiaxed grain structure. Duration of such annealing treatment has to be limited to avoid undesirable grain growth. Annealing at 440 °C for 3 h was chosen according to previous investigations. After annealing and cooling in air, the plates were cut to the dimensions of 140 × 50 mm. FSP was conducted using a milling machine equipped with a cylindrical tool with a shoulder diameter of 15 mm and a pin height of 2.5 mm and a pin diameter of 3.5 mm (Fig. 1). The tool displaced at a moving speed of 107 mm/min and a rotation speed 180 rpm, which were chosen, based on the previous experimental research [68,69]. To investigate the effect of the cumulative deformation on the microstructure, mechanical properties and corrosion resistance of the alloy, multiple FSP passes, i.e., 1, 2, 4 and 6, were applied to the as-annealed alloy. The repetitive passes of FSP were conducted on one specific sample to acquire sufficiently processed samples. In each case, the first pass was applied clock-wise and the second pass counter clock-wise, which was successively continued.

Table 1 – Chemical composition of the WE43 magnesium alloy used as the experimental material in this investigation.

Element	Mg	Zn	Y	Zr	Sc	Ce	Nd	Gd
Wt. %	Balance	0.08	4.28	0.41	1.47	0.13	0.74	0.28

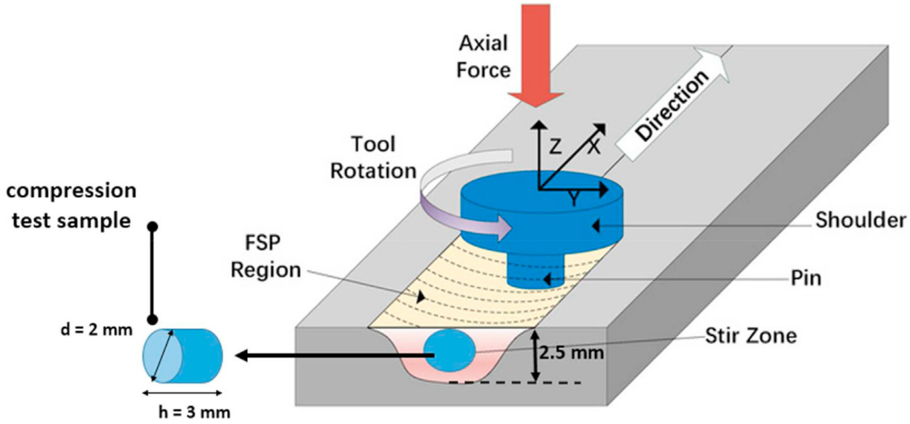

Fig. 1 – Schematic illustration of FSP and the region where samples were extracted.

Samples for microstructural analysis were extracted from the region below the surface along the FSP centerline (Fig. 1). An HUVITZ HR3-TRF-P optical microscope was used to examine the grain structures after different passes of FSP. Prior to microscopy, the samples were ground, polished and etched. The etchant was a solution composed of 5 ml acetic acid, 5 g picric acid, 100 ml ethanol and 10 ml distilled water. TESCAN VEGA/XMU and Philips XL30S-FEG SEM microscopes were used to determine the sizes, morphology and distributions of second-phase particles. Electron backscatter diffraction (EBSD) was used to reveal the effect of FSP on grain refinement. Samples were ground and electro-polished at 20 V in a 300 ml HNO_3 + 700 ml C_2H_5OH solution at −35 °C. EBSD micrographs were taken using a Philips XL30S-FEG SEM microscope.

Compression tests were performed, using a 5-ton SANTAM universal tensile/compression machine at a crosshead speed of 0.5 mm/min to investigate the effect of FSP on the mechanical properties of specimens. Cylindrical specimens with a diameter of 2 mm diameter and a height of 3 mm, according to the ASTM E9 standard, were prepared from the region below the surface along the centerline of FSP (Fig. 1).

Potentiodynamic polarization tests and electrochemical impedance spectroscopy (EIS) were performed to investigate the effect of FSP on the corrosion properties of the alloy. The polarization tests were conducted in simulated body fluid (SBF) solution according to the ASTM G102-98-E1 standard, using a Princeton Applied Research potentiostat apparatus (Versa Stat 4) with a three-electrode electrochemical cell at room temperature. Sample with a surface area of 10 mm^2 was set as the working electrode and the counter and reference electrodes were platinum rod and saturated calomel, respectively. Scans were done at a rate of 1 mV/S and started at −0.25 V below open circuit potential (OCP) and finished at a reference electrode potential (SCE). Corrosion current density and corrosion potential were calculated using the TOEFL extrapolation of the anodic and cathodic branches. Electrochemical impedance spectrometry (EIS) was performed in SBF solution, according to ASTMB457-67, over a range of applied frequency from 10 mHz to 100 KHz. The amplitude of voltage was 10 mV. Experimental results were fitted by using the ZSimWin 3.21 software.

3. Results and discussion

3.1. Evolution of microstructure

3.1.1. Initial microstructure

The as-annealed microstructure of the WE43 alloy is shown in Fig. 2. An equiaxed grain structure was observed, which could be attributed to dynamic crystallization occurring during hot rolling and subsequent grain growth during annealing. The average grain size was calculated, according to the ASTM E-112 standard, to be 12.4 μm. A continuous network of second-phase particles was present at the grain boundaries (Fig. 2a). In the as-annealed WE43 alloy, these particles are known to be binary intermetallic compounds of Mg–Nd and Mg–Y [70] or ternary intermetallic compounds of Mg-Nd-Y [71], of high hardness and strength, and a main contributor to reduced ductility and deformability of the alloy. The distribution of intermetallic particles at the grain boundaries imposes additional restrictions to the deformation of the alloy which has an HCP crystal structure and an inherently low number of slip systems at room temperature [72–77]. In addition to the second-phase particles at the grain boundaries, a large number of intermetallic particles in the needle shape (Fig. 2b) were distributed inside the grains, which would also contribute to reduced ductility.

3.1.2. Macrostructures of the alloy after multi-pass FSP

The material subjected to FSP has varied thermal and mechanical histories. The FSP region on the cross section can be divided into the stir zone (SZ), thermo-mechanically affected zone (TMAZ), heat affected zone (HZ) and the base metal (BM) which is not affected by FSP. The width, depth and direction of

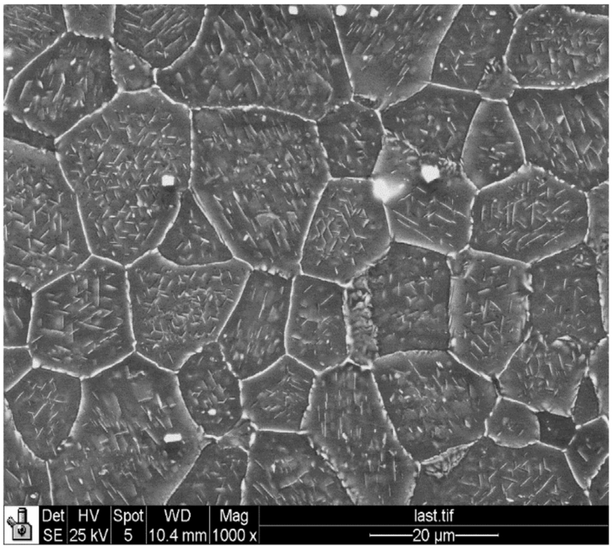

(a)

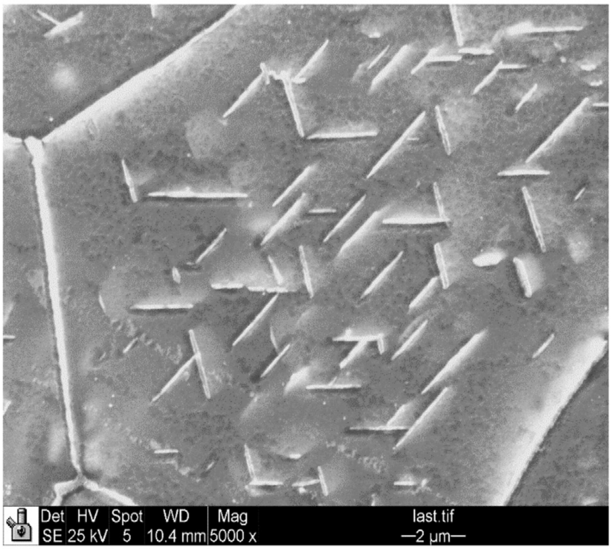

(b)

Fig. 2 – The as-annealed microstructure of the WE43 alloy showing (a) the grain structure and (b) the distribution of second-phase particles.

these zones depend mainly on process parameters, i.e., tool rotation speed and moving speed and on tool design [58]. These zones may undergo small changes at successive FSP passes. The effect of the successive FSP passes on the shape and extent of the FSP zones in the WE43 alloy are shown in Fig. 3. It can be seen that the FSP region in general had the shape of a spherical cap with a width of 15 mm and a depth of 3 mm. This region did not significantly change with rising FSP passes. However, the extent of the SZ zone, being the main part stirred during FSP, was changed. Compared to the other zones, SZ was subjected to the maximum amount of deformation, had the finest grain sizes and experienced particle fragmentation and redistribution the most [78–80]. Therefore, this zone was selected to investigate the effect of FSP on the microstructure, mechanical properties and corrosion resistance of the alloy.

3.1.3. *Evolution of grain structure in the stir zone (SZ)*

EBSD micrographs showing the grain structures of the SZ samples after 1, 2, 4 and 6 passes of FSP are presented in Fig. 4. Progressive reduction in grain size indeed occurred during FSP. The average values of grain size, measured according to ASTM E112, were 5.47, 2.47, 1.43 and 1.41 μm with an error range of 5%. Comparison of these values with the average grain size of the as-annealed material (12.4 μm) indicated 56 and 80% reductions in average grain size because of the first pass and second passes of FSP. With further deformation, grain refinement continued to reach a minimum value of 1.4 μm, which was about an 85% reduction from the as-annealed grain size. Such a significant reduction in grain size could significantly contribute to increasing ductility and strength of the alloy. The differences between the average grain size values after 4 and 6 passes of FSP, however, fell within the margin of error. In other words, grain refinement reached the ceiling after 4 passes of FSP.

3.1.4. *Evolution of second-phase particles*

The effect of FSP on the sizes, morphology and distribution of second phase particles is depicted in Fig. 5. In comparison with the as-annealed microstructure with a continuous network of second-phase particles at the grain boundaries and a high density of needle-shaped particles in the grain interior, the second-phase particles became fragmented and redistributed inside the grains. The needle-shaped particles were not observable in the grain interior any more, after two passes of FSP were applied. In addition, the linkage and continuity of the particles at the grain boundaries were destroyed, with some residuals still visible. Along with further FSP, i.e., 4 passes, the remaining grain boundary particles were further redistributed in the grain interior and fragmented into finer sizes. In the sample having experienced 6 passes of FSP, extra-fine second-phase particles were hardly discernible at the same magnification under SEM (Fig. 5d).

3.2. *Mechanical properties*

The compression stress–strain curves of specimens in the as-annealed state and after 1, 2, 4 and 6 passes of FSP are shown in Fig. 6. Since the specimens were not supposed to show necking in compression testing and consequently reduced stress, the uniform strain to maximum stress (ε_u) was chosen to represent the ductility of the specimens after SFP. For the as-annealed WE43 alloy, the uniform strain at the maximum compressive strength of 206 MPa was only 0.026, showing poor ductility. After the first pass of FSP was applied, the maximum strength reached 227 MPa, while the uniform strain remained unchanged. With two passes of FSP applied, the ε_u value increased to 0.05%, which was a 100% increase, and the maximum compressive strength reached 250 MPa. With further FSP to 4 passes, about a 50% further increase in ε_u and a 10% increase in compressive strength were achieved. This upward trend continued to $\varepsilon_u = 0.1$, after 6 passes of FSP were

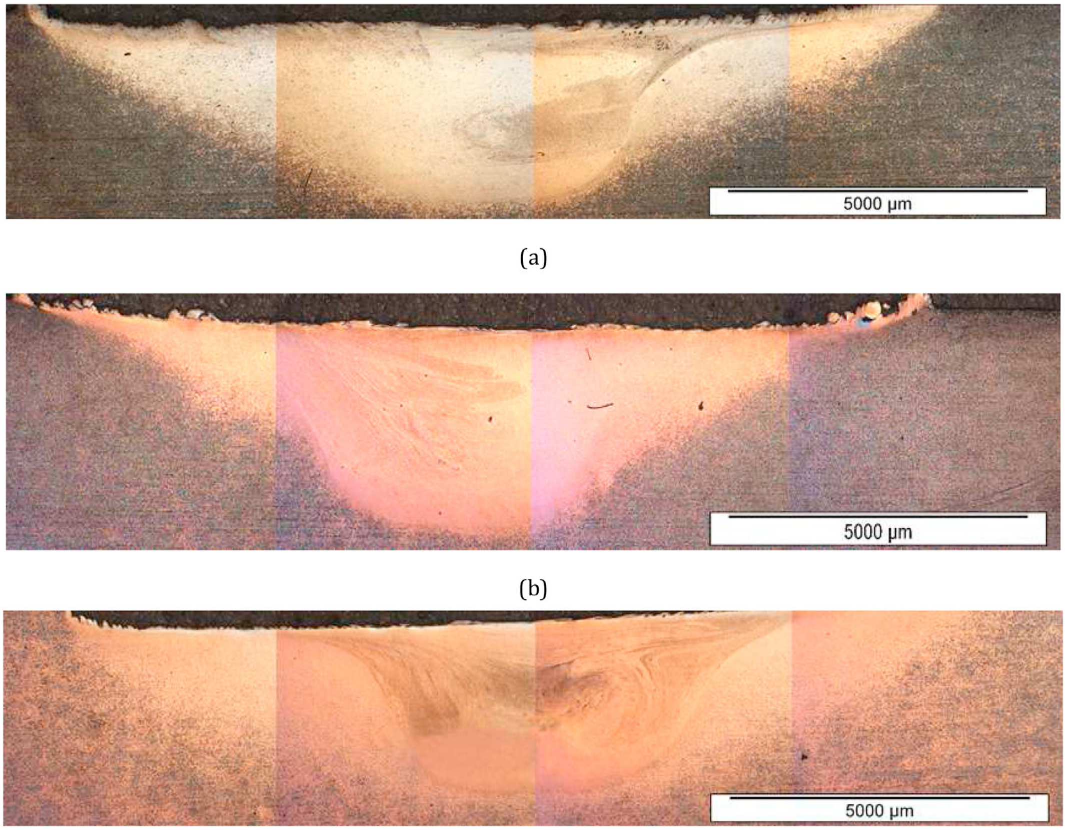

(c)

Fig. 3 – Macrostructures of the FSP samples after (a) 2, (b) 4 and (c) 6 passes.

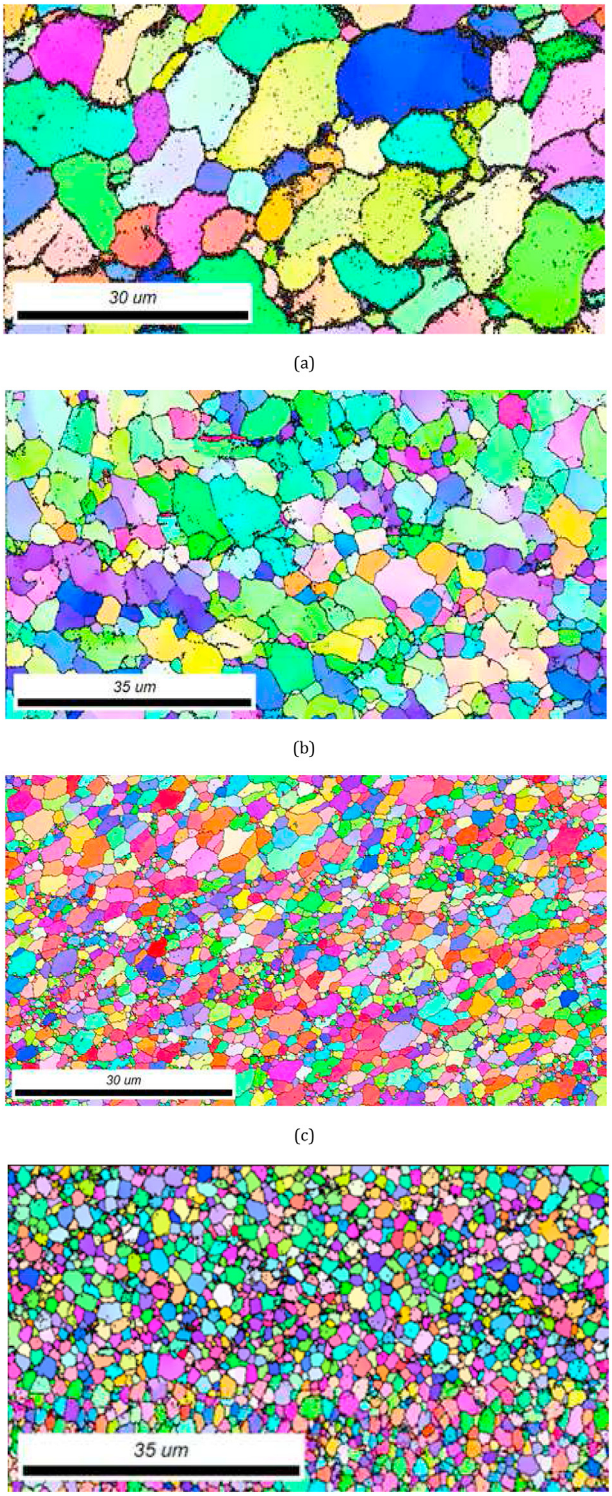

(a)

(b)

(c)

(d)

Fig. 4 – EBSD maps showing the grain structures of the FSP SZ samples after (a) 1 pass, (b) 2 passes, (c) 4 passes and (d) 6 passes of FSP.

applied, while the maximum compressive strength remained unchanged at 277 MPa. Therefore, the application of 6 passes of FSP resulted in a 4-fold increase in uniform strain to maximum stress and a 35% enhancement in compressive strength.

The increase in ductility after 2 passes of FSP could be attributed mainly to the significant grain refinement. With a further increase in FSP pass, further grain refinement occurred in addition to the fragmentation of second-phase particles. A continuous network of particles at the grain boundaries would seriously limit the ductility of the alloy which is inherently low due to a limited number of slip systems in the α-Mg matrix at room temperature [75–77]. Normally, for a metal with an HCP crystal structure, grain boundaries can be of help in enlarging its ductility, due to an increased number of slip systems in their vicinity [75–77]. When the grain boundary regions are occupied by a continuous network of second-phase particles, however, the constructive effect of grain boundaries on ductility will severely diminish [75–77]. Furthermore, most of intermetallic compounds themselves are of low ductility and high strength, as compared to the matrix. Usually, they do not deform as much as the matrix, which may result in discontinuity between the particles and matrix, and the formation of crack initiation points. Consequently, very poor ductility of an HCP-structured metal with a network of intermetallic compounds at the grain boundaries can be expected. However, when the particles become fragmented and redistributed inside grains, the grain boundaries will offer increased ductility to the metal due to a larger number of slip systems. Moreover, crack initiation points at the vicinities of particles are fewer in number, as they are finer and discontinuous. Therefore, improved ductility can be achieved.

3.3. *Corrosion behavior*

3.3.1. *Potentiodynamic polarization*

The potentiodynamic polarization curves of the samples in the as-annealed state and after 6 passes of FSP are shown in Fig. 7. The values of I_{corr} (corrosion current density), E_{corr} (corrosion potential versus that of SC electrode), β_a (the slope of anodic branch), β_c (the slope of cathodic branch) and CR (the corrosion rate) were calculated by using the versaSTAT4 software. All the electrochemical polarization parameters are listed in Table 2. In addition, the value of R_p (polarization resistance) was calculated using the Stern–Geary equation (Eq. (1)) [81]:

$$R_p = \frac{1}{2.303\left(\frac{1}{\beta a} + \frac{1}{\beta c}\right) i_{corr}} \tag{1}$$

It can be seen that by applying 6 passes of FSP to the WE43 alloy, the values of I_{corr} and CR decreased and R_p increased significantly. FSP was found to have both negative and positive effects on the corrosion of the alloy. In general, two factors strongly affect the corrosion behavior of the WE43 alloy, i.e., grain sizes and the sizes, surface fraction and distribution of second-phase particles. Finer grains result in a higher density of grain boundaries that are the corrosion-prone region owing to their high energy. In addition, second-phase particles may cause a higher corrosion rate because they are inherently different from the matrix in corrosion potential and can form galvanic cells, resulting in galvanic corrosion

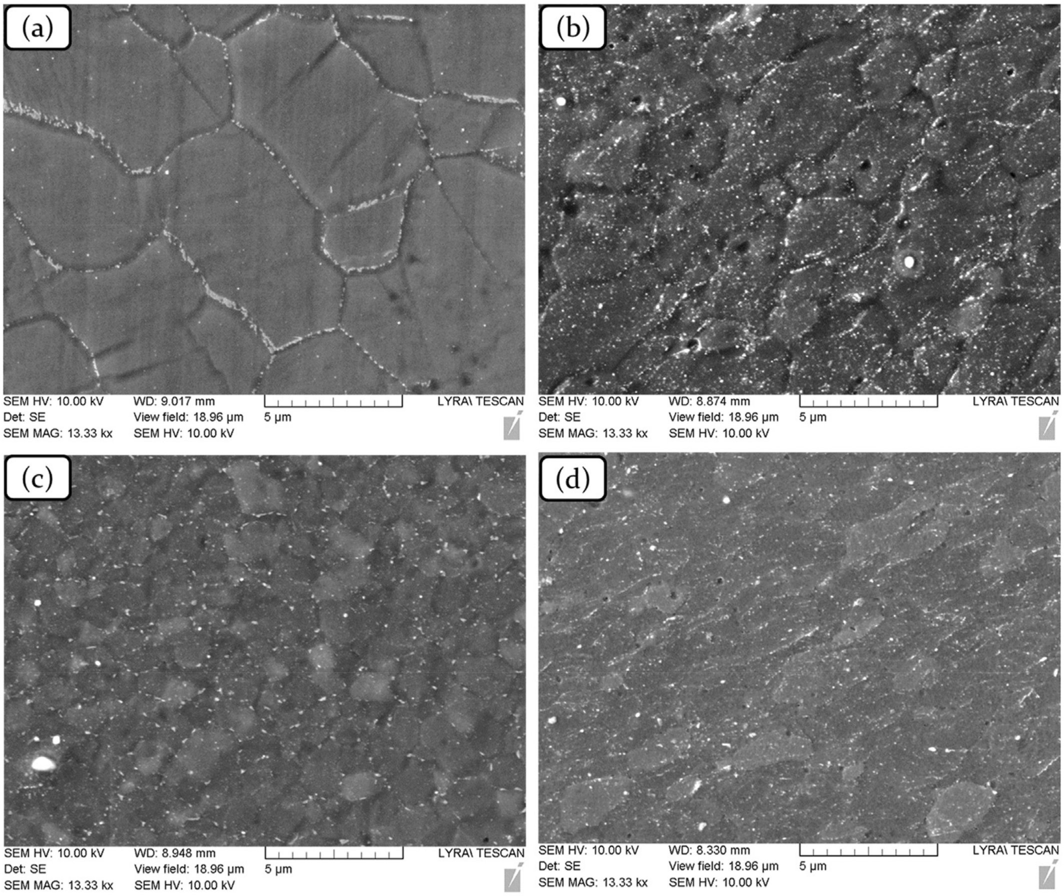

Fig. 5 – SEM images showing the second phase particles in the FSP-processed samples after (a) 1, (b) 2, (c) 4 and (d) 6 passes.

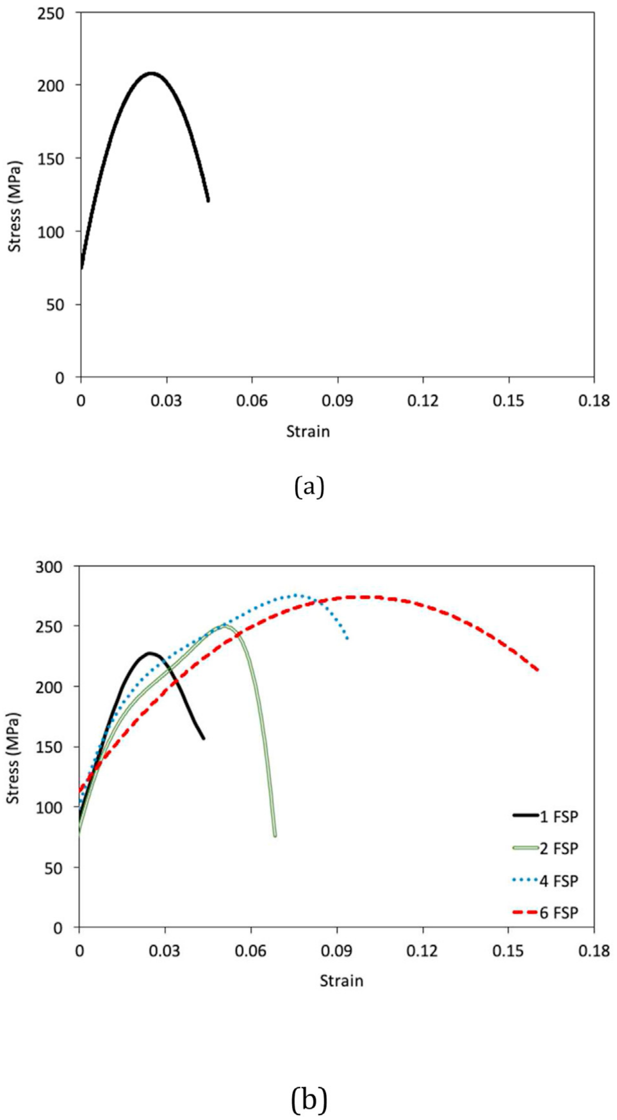

(a)

(b)

Fig. 6 – Stress–strain curves of specimens in the (a) as-annealed state and (b) after multi-pass FSP.

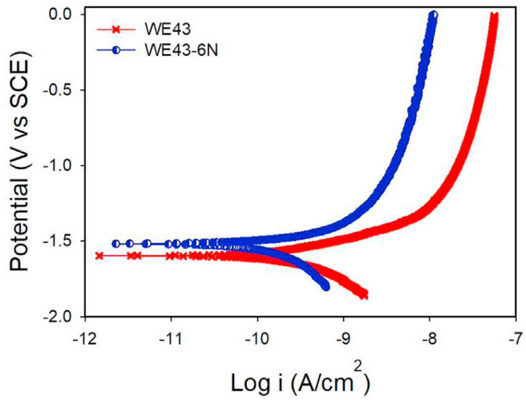

Fig. 7 – The potentiodynamic polarization curves of the as-annealed WE43 alloy and the same alloy after 6 pass FSP.

and the formation of initial pits for pitting corrosion to proceed.

After six passes of FSP, significant grain refinement took place, as seen Fig. 4. The average grain size reduced from 12.4 to 1.5 μm, which could cause a significant increase in the density of grain boundaries and consequently a higher corrosion rate. An increase in corrosion rate after different processes of SPD has been observed in different alloy systems [82–90]. However, in the case of the current alloy, due to effective fragmentation and redistribution of second-phase particles (Fig. 5) along with FSP, the preferred sites for localized corrosion at the grain boundaries were decreased, which led to a reduced corrosion rate by changing the thermodynamics and kinetics of corrosion, as demonstrated by the CR values in Table 2. Because of the reduction in second-phase particle sizes and the redistribution of these particles, the differences in corrosion rate between anodic and cathodic reactions and the intensity of microscopic galvanic coupling were decreased. As a result, the main corrosion mechanism changed towards more uniform corrosion. The negative effects of increased grain boundaries and densities became much less than the positive effect of fragmented second-phase particles. As explained earlier, in this case, the second-phase particles would be so severely refined that they might also be dissolved in many alloy systems [91–93] or in magnesium alloys [94]. Irrespective of being dissolved or significantly reduced in size, they lost their detrimental effect to act as preferred sites for localized corrosion. Consequently, applying FSP led to the changes in corrosion behavior and the kinetic aspect of corrosion, and to an increase in pitting corrosion resistance. Consequently, the formed pits on the surface became less stable and could re-passivate, causing more uniform corrosion.

3.3.2. *EIS analysis*

The Nyquist, bode and bode phase diagrams of the WE43 alloy in the as-annealed state and after 6 passes of FSP are shown in Fig. 8. It can be seen in Fig. 8 (a) that the Nyquist diagram includes two positive capacitive arcs and one negative inductive arc. One of the two capacitive arcs must have been correlated to the passive layer that was generated near the surface of the sample and indicated its corrosion resistance. The other one was correlated to the transition of electrical charge at the metal/electrolyte interface (i.e., a double electrical layer). In addition, the negative inductive arc was related to the inductive behavior of pits at low frequencies.

After fitting the experimental EIS data by using the ZSimWin 3.21 software, the simulated equivalent circuit was found to be R_{sol} (C_PR_P) (Q_{dl} (R_t ($L_{Pit}R_{Pit}$))). In the obtained equivalent circuit, R_{sol} is the electrical resistance of the SBF solution, C_p and R_p are the electrical capacitive behavior and electrical resistance of the passive layer, respectively. L_{pit} and R_{pit} represent the inductive behavior of pits that may be related to second-phase particles, Q_{dl} is the electrical capacitive behavior of the double electrical layer and R_t is the charge transfer resistance of the substrate-passive layer interface. The values of these EIS parameters were calculated from the experimental EIS data and are reported in Table 3. There was a good agreement between the measured data and the fitted data, meaning that a convenient equivalent circuit was

Table 2 – Calculated electrochemical polarization parameters of the as-annealed WE43 alloy and the same alloy after 6 passes of FSP.

Sample	I_{Corr} (μA/cm^2)	E_{Corr} (V vs SCE)	β_a(mV.dec^{-1})	-βc (mV.dec^{-1})	RP (ohm./cm^{2}I/cm^{2}Icm2Icm2)	CR (mm/y)
WE43	215.372	−1.585	147.932	253.297	188.285	3.994
WE43-6 N	133.951	−1.515	129.433	344.751	305.045	2.484

chosen and the fitting performed by the software was adequate. The values of fitting process error (K_{square}) for the WE43 alloy in the as-annealed state and after 6 passes of FSP were 3.01 × 10^{-5} and 1.72 × 10^{-5}, respectively. The equivalent circuit includes a constant phase element (CPE) parameter for the double electrical layer, in which CPE_{dl} indicates the dielectric properties of the double electrical layer that represents the amount of deviation from the ideal capacitive behavior and the inhomogeneity of the sample surface [95].

It is known that larger capacitive and inductive arcs indicate higher corrosion resistance. As can be seen in Fig. 8a, the capacitive arc diameter enlarged and corrosion resistance increased, due to FSP. As previously explained, the fragmentation of second-phase particles contributed to the increased corrosion resistance of the alloy after FSP. There is no specific or clear definition of the inductive loop, but it may be correlated to the generation and re-passivation of pits on the surface due to the participation of second-phase particles in localized corrosion. The WE43 alloy after 6 passes of FSF exhibited a larger inductive arc diameter, higher pitting resistance and fewer stable pits. In fact, because of the small sizes of the generated pits in the WE43 alloy after 6 passes of FSP, the intensity of micro galvanic coupling was reduced and re-passivation of pits increased. In addition, the corrosive reactions on the surface became more uniform and caused the creation of a more uniform oxide/hydroxide passive layer on the surface. Also, the values of R_{pit}, L_{pit} and R_t increased, which could result from a uniform passive layer surrounding fragmented particles and resulted in increased inductive resistance and decreased pitting corrosion.

In Fig. 8b, the slope of the linear portion of the bode curves, *n*, at high frequencies, can be taken as an acceptable parameter for evaluating the corrosion properties of samples with respect to the uniformity of the formed passive layer on surface [96]. By improving the protective properties of the passive layer, the *n* value is increased towards one. By applying FSP to the WE43 alloy, the *n* value was indeed increased, indicating a more uniform and smoother passive layer and a better protective effect (nWE43 < nWE43-6 N). Thus, the formed passive layer on the WE43 alloy after 6 passes of FSP could more effectively prevent the detrimental and corrosive electrochemical reactions on the surface from taking place.

Furthermore, the single capacitive peak in the bode phase (Fig. 8c) diagrams is a precise and good parameter for the evaluation of the corrosion behavior of the metal substrate. The highest peak in the bode phase diagrams is related to the roughness of the substrate [96]. As clearly visible in the curves, the highest peak was increased by applying FSP, which could be correlated to the higher roughness of WE43-6 N sample surface. In this sample, high density and fine sizes of second-phase particles could be of help for surface protection.

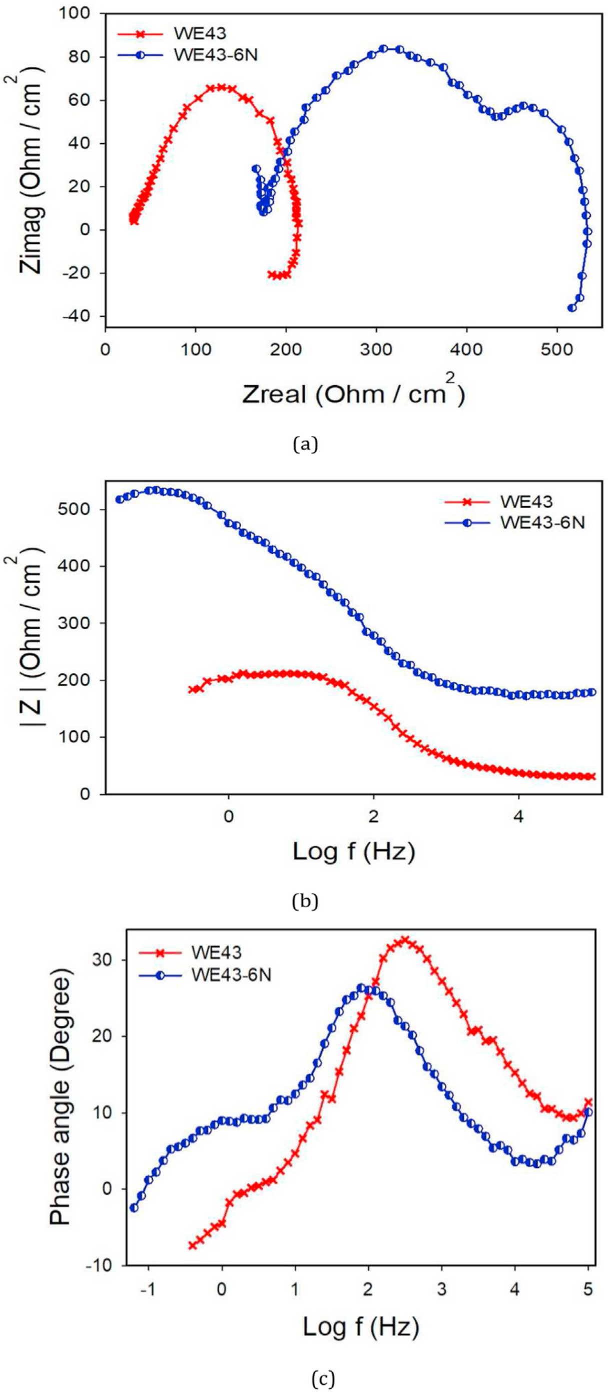

Fig. 8 – (a) The Nyquist, (b) the bode and (c) the bode phase curves of the WE43 alloy in the as-annealed state and after 6 passes of FSP.

Table 3 – The calculated EIS parameters from the experimental EIS data.

Sample	R_{sol} (Ohm/cm^2)	$(Q\text{-}m)_{dl}$	R_{dl} (Ohm/cm^2)	R_{pit} (Ohm/cm^2)	L_{pit} (H/cm^2)	K_{square}
WE43	24.63	0.88	281.72	21.81	140.92	3.01×10^{-5}
WE43-6 N	24.69	0.74	368.94	37.03	233.88	1.72×10^{-5}

4. Conclusions

In this research, the effect of FSP on the evolution of microstructure, mechanical properties and corrosion behavior of the WE43 magnesium alloy with increasing number of FSP passes was investigated. Based on the results obtained, the following conclusions could be drawn.

1) By applying FSP, a significant reduction in grain size occurred. The average grain size was reduced from an initial value of 12.4 to 2.5 μm after 2 passes of FSP. With further FSP to 4 passes, the average grain size was reduced to 1.43 μm, which remained stable with further increase in FSP pass to 6.
2) Significant second-phase particle fragmentation was observed as a result of applying two passes of FSP. Further FSP could effectively fragment and redistribute these particles.
3) The improvement in the strength of the alloy by applying FSP could be attributed to the reduction in grain size. As the average grain size reached a stable value after 4 passes of FSP, the strength and ductility continued to increase with increasing number of FSP passes. This was attributed to the further fragmentation and improved distribution of second-phase particles.
4) Corrosion resistance of the alloy was found to improve by applying 6 passes of FSP. By applying FSP, pitting corrosion resistance and uniformity of protective passive layer were improved and the intensity of micro galvanic coupling was decreased.

Declaration of Competing Interest

I declare the authors have no competing interests as defined by Nature Research, or other interests that might be perceived to influence the interpretation of the article.

REFERENCES

[1] Poinern GEJ, Brundavanam S, Fawcett D. Biomedical magnesium alloys: a review of material properties, surface modifications and potential as a biodegradable orthopaedic implant. Am J Biomed Eng 2012;2(6):218–40.
[2] Gu X-N, Zheng Y-F. A review on magnesium alloys as biodegradable materials. Front Mater Sci China 2010;4(2):111–5.
[3] Li N, Zheng Y. Novel magnesium alloys developed for biomedical application: a review. J Mater Sci Technol 2013;29(6):489–502.
[4] Jones TL, Kondoh K. Ballistic analysis of new military grade magnesium alloys for armor applications. Magnesium technology 2011. Springer; 2011. p. 425–30.
[5] Jones TL, Labukas JP, Placzankis BE, Kondoh K. Ballistic and corrosion analysis of new military-grade magnesium alloys AMX602 and ZAXE1711 for armor applications. ARMY RESEARCH LAB ABERDEEN PROVING GROUND MD WEAPONS AND MATERIALS RESEARCH; 2012.
[6] Mathaudhu S, Nyberg E, Wmm-F APG. Magnesium alloys in army applications: past, current and future solutions. 14-18 feb. Minerals, Metals and Materials Society/AIME, 420 Commonwealth Dr., P. O. Box. In: Minerals, metals and materials society/AIME, 420 commonwealth Dr., P. O. Box 430 warrendale PA 15086 USA; 2010.
[7] Mathaudhu SN, Nyberg EA. Magnesium alloys in US military applications: past, current and future solutions. Richland, WA (United States): Pacific Northwest National Lab.(PNNL); 2010.
[8] Monteiro WA, Buso SJ, Silva LV. Application of magnesium alloys in transport. New Featur Magnes Alloys 2012:1–14.
[9] Göken J, Bohlen J, Hort N, Letzig D, Kainer KU. New development in magnesium technology for light weight structures in transportation industries. Materials science forum. Trans Tech Publ; 2003. p. 153–60.
[10] Pollock TM. Weight loss with magnesium alloys. Science 2010;328(5981):986–7.
[11] Kulekci MK. Magnesium and its alloys applications in automotive industry. Int J Adv Manuf Technol 2008;39(9–10):851–65.
[12] Easton M, Beer A, Barnett M, Davies C, Dunlop G, Durandet Y, et al. Magnesium alloy applications in automotive structures. JOM (J Occup Med) 2008;60(11):57.
[13] Bettles C, Gibson M. Current wrought magnesium alloys: strengths and weaknesses. JOM (J Occup Med) 2005;57(5):46–9.
[14] Mö P, Mm A. Magnesium alloying, some potentials for alloy development. J Jpn Inst Light Met 1992;42(12):679–86.
[15] Polmear IJ. Magnesium alloys and applications. Mater Sci Technol 1994;10(1):1–16.
[16] Makar GL, Kruger J. Corrosion of magnesium. Int Mater Rev 1993;38(3):138–53.
[17] Song G-L. Corrosion of magnesium alloys. Elsevier; 2011.
[18] Gusieva K, Davies CHJ, Scully JR, Birbilis N. Corrosion of magnesium alloys: the role of alloying. Int Mater Rev 2015;60(3):169–94.
[19] Ghali E, Dietzel W, Kainer K-U. General and localized corrosion of magnesium alloys: a critical review. J Mater Eng Perform 2004;13(1):7–23.
[20] Zeng R, Zhang J, Huang W, Dietzel W, Kainer KU, Blawert C, et al. Review of studies on corrosion of magnesium alloys. Trans Nonferrous Met Soc China 2006;16:s763–71.
[21] Kang F, Li Z, Wang JT, Cheng P, Wu HY. The activation of< c+a> non-basal slip in magnesium alloys. J Mater Sci 2012;47(22):7854–9.
[22] Koike J, Kobayashi T, Mukai T, Watanabe H, Suzuki M, Maruyama K, et al. The activity of non-basal slip systems and dynamic recovery at room temperature in fine-grained AZ31B magnesium alloys. Acta Mater 2003;51(7):2055–65.
[23] Kim WJ, Jeong HG, Jeong HT. Achieving high strength and high ductility in magnesium alloys using severe plastic

deformation combined with low-temperature aging. Scripta Mater 2009;61(11):1040–3.
[24] Zhang H, Huang G, Wang L, Roven HJ, Xu Z, Pan F. Improved ductility of magnesium alloys by a simple shear process followed by annealing. Scripta Mater 2013;69(1):49–52.
[25] Lukáč P, Trojanová Z. Influence of grain size on ductility of magnesium alloys. Mater Eng 2011;18:110–4.
[26] Del Valle JA, Carreño F, Ruano OA. Influence of texture and grain size on work hardening and ductility in magnesium-based alloys processed by ECAP and rolling. Acta Mater 2006;54(16):4247–59.
[27] Wu Z, Ahmad R, Yin B, Sandlöbes S, Curtin WA. Mechanistic origin and prediction of enhanced ductility in magnesium alloys. Science 2018;359(6374):447–52.
[28] Wu Z, Curtin WA. The origins of high hardening and low ductility in magnesium. Nature 2015;526(7571):62–7.
[29] Barnett MR. Twinning and the ductility of magnesium alloys: Part II."Contraction" twins. Mater Sci Eng, A 2007;464(1–2):8–16.
[30] Xie J, Li Q, Wang X-Q, Li J-H. Microstructure and mechanical properties of AZ81 magnesium alloy with Y and Nd elements. Trans Nonferrous Met Soc China 2008;18(2):303–8.
[31] Xiaoqin Z, Qudong W, Yizhen L, Yanping Z, Wenjiang D, Yunhu Z. Influence of beryllium and rare earth additions on ignition-proof magnesium alloys. J Mater Process Technol 2001;112(1):17–23.
[32] Masoudpanah SM, Mahmudi R. Effects of rare-earth elements and Ca additions on the microstructure and mechanical properties of AZ31 magnesium alloy processed by ECAP. Mater Sci Eng, A 2009;526(1–2):22–30.
[33] Hirai K, Somekawa H, Takigawa Y, Higashi K. Effects of Ca and Sr addition on mechanical properties of a cast AZ91 magnesium alloy at room and elevated temperature. Mater Sci Eng, A 2005;403(1–2):276–80.
[34] Khomamizadeh F, Nami B, Khoshkhooei S. Effect of rare-earth element additions on high-temperature mechanical properties of AZ91 magnesium alloy. Metall Mater Trans 2005;36(12):3489–94.
[35] Cheng Y, Qin T-W, Wang H-M, Zhang Z. Comparison of corrosion behaviors of AZ31, AZ91, AM60 and ZK60 magnesium alloys. Trans Nonferrous Met Soc China 2009;19(3):517–24.
[36] Zhao M-C, Liu M, Song G, Atrens A. Influence of the β-phase morphology on the corrosion of the Mg alloy AZ91. Corrosion Sci 2008;50(7):1939–53.
[37] Ali Y, Qiu D, Jiang B, Pan F, Zhang M-X. Current research progress in grain refinement of cast magnesium alloys: a review article. J Alloys Compd 2015;619:639–51.
[38] StJohn DH, Qian MA, Easton MA, Cao P, Hildebrand Z. Grain refinement of magnesium alloys. Metall Mater Trans 2005;36(7):1669–79.
[39] Qian M, Das A. Grain refinement of magnesium alloys by zirconium: formation of equiaxed grains. Scripta Mater 2006;54(5):881–6.
[40] Cao P, Qian M, StJohn DH. Native grain refinement of magnesium alloys. Scripta Mater 2005;53(7):841–4.
[41] Ramirez A, Qian M, Davis B, Wilks T, StJohn DH. Potency of high-intensity ultrasonic treatment for grain refinement of magnesium alloys. Scripta Mater 2008;59(1):19–22.
[42] Lee YC, Dahle AK, StJohn DH. The role of solute in grain refinement of magnesium. Metall Mater Trans 2000;31(11):2895–906.
[43] Ji YH, Park JJ. Analysis of thermo-mechanical process occurred in magnesium alloy AZ31 sheet during differential speed rolling. Mater Sci Eng, A 2008;485(1–2):299–304.
[44] El-Morsy A, Ismail A, Waly M. Microstructural and mechanical properties evolution of magnesium AZ61 alloy processed through a combination of extrusion and thermomechanical processes. Mater Sci Eng, A 2008;486(1–2):528–33.
[45] Kumar NR, Blandin JJ, Desrayaud C, Montheillet F, Suéry M. Grain refinement in AZ91 magnesium alloy during thermomechanical processing. Mater Sci Eng, A 2003;359(1–2):150–7.
[46] Zhao Z, Chen Q, Hu C, Shu D. Microstructure and mechanical properties of SPD-processed an as-cast AZ91D+ Y magnesium alloy by equal channel angular extrusion and multi-axial forging. Mater Des 2009;30(10):4557–61.
[47] Kai M, Horita Z, Langdon TG. Developing grain refinement and superplasticity in a magnesium alloy processed by high-pressure torsion. Mater Sci Eng, A 2008;488(1–2):117–24.
[48] Yamashita A, Horita Z, Langdon TG. Improving the mechanical properties of magnesium and a magnesium alloy through severe plastic deformation. Mater Sci Eng, A 2001;300(1):142–7.
[49] Fatemi-Varzaneh SM, Zarei-Hanzaki A. Processing of AZ31 magnesium alloy by a new noble severe plastic deformation method. Mater Sci Eng, A 2011;528(3):1334–9.
[50] Figueiredo RB, Langdon TG. Principles of grain refinement and superplastic flow in magnesium alloys processed by ECAP. Mater Sci Eng, A 2009;501(1–2):105–14.
[51] Fatemi-Varzaneh SM, Zarei-Hanzaki A, Cabrera JM, Calvillo PR. EBSD characterization of repetitive grain refinement in AZ31 magnesium alloy. Mater Chem Phys 2015;149:339–43.
[52] Figueiredo RB, Langdon TG. Principles of grain refinement in magnesium alloys processed by equal-channel angular pressing. J Mater Sci 2009;44(17):4758–62.
[53] Chen Q, Shu D, Hu C, Zhao Z, Yuan B. Grain refinement in an as-cast AZ61 magnesium alloy processed by multi-axial forging under the multitemperature processing procedure. Mater Sci Eng, A 2012;541:98–104.
[54] Sivakesavam O, Rao IS, Prasad Y. Processing map for hot working of as cast magnesium. Mater Sci Technol 1993;9(9):805–10.
[55] Wang CY, Wang XJ, Chang H, Wu K, Zheng MY. Processing maps for hot working of ZK60 magnesium alloy. Mater Sci Eng, A 2007;464(1–2):52–8.
[56] Xu Y, Hu L, Deng T, Ye L. Hot deformation behavior and processing map of as-cast AZ61 magnesium alloy. Mater Sci Eng, A 2013;559:528–33.
[57] Zhou HT, Li QB, Zhao ZK, Liu ZC, Wen SF, Wang QD. Hot workability characteristics of magnesium alloy AZ80—a study using processing map. Mater Sci Eng, A 2010;527(7–8):2022–6.
[58] Wang W, Han P, Peng P, Zhang T, Liu Q, Yuan S-N, et al. Friction stir processing of magnesium alloys: a review. Acta Metall Sin Engl Lett 2020;33(1):43–57.
[59] Yang Q, Xiao BL, Ma ZY, Chen RS. Achieving high strain rate superplasticity in Mg–Zn–Y–Zr alloy produced by friction stir processing. Scripta Mater 2011;65(4):335–8.
[60] Chang CI, Du XH, Huang JC. Achieving ultrafine grain size in Mg–Al–Zn alloy by friction stir processing. Scripta Mater 2007;57(3):209–12.
[61] Feng AH, Ma ZY. Enhanced mechanical properties of Mg–Al–Zn cast alloy via friction stir processing. Scripta Mater 2007;56(5):397–400.
[62] Cavaliere P, De Marco PP. Friction stir processing of AM60B magnesium alloy sheets. Mater Sci Eng, A 2007;462(1–2):393–7.
[63] Darras BM, Khraisheh MK, Abu-Farha FK, Omar MA. Friction stir processing of commercial AZ31 magnesium alloy. J Mater Process Technol 2007;191(1–3):77–81.
[64] Zhang D-T, Xiong F, Zhang W-W, Cheng QIU, Zhang W. Superplasticity of AZ31 magnesium alloy prepared by

friction stir processing. Trans Nonferrous Met Soc China 2011;21(9):1911–6.

[65] Zeng R-C, Chen J, Dietzel W, Zettler R, dos Santos JF, Nascimento ML, et al. Corrosion of friction stir welded magnesium alloy AM50. Corrosion Sci 2009;51(8):1738–46.

[66] Argade GR, Kandasamy K, Panigrahi SK, Mishra RS. Corrosion behavior of a friction stir processed rare-earth added magnesium alloy. Corrosion Sci 2012;58:321–6.

[67] Behnagh RA, Besharati Givi MK, Akbari M. Mechanical properties, corrosion resistance, and microstructural changes during friction stir processing of 5083 aluminum rolled plates. Mater Manuf Process 2012;27(6):636–40.

[68] Charit I, Mishra RS. Abnormal grain growth in friction stir processed alloys. Scripta Mater 2008;58(5):367–71.

[69] Attallah MM, Salem HG. Friction stir welding parameters: a tool for controlling abnormal grain growth during subsequent heat treatment. Mater Sci Eng, A 2005;391(1–2):51–9.

[70] Rzychoń T, Kie∖lbus A. Microstructure of WE43 casting magnesium alloys. J Achiev Mater Manuf Eng 2007;21(1):31–4.

[71] Jiang HS, Zheng MY, Qiao XG, Wu K, Peng QY, Yang SH, et al. Microstructure and mechanical properties of WE43 magnesium alloy fabricated by direct-chill casting. Mater Sci Eng, A 2017;684:158–64.

[72] Polesak FJ, Davis B, DeLorme R, Agnew SR. Hot workability of alloy WE43 examined using hot torsion testing. Magnesium technology 2011. Springer; 2011. p. 379–84.

[73] Kang Y, Huang Z, Zhao H, Gan C, Zhou N, Zheng K, et al. Comparative study of hot deformation behavior and microstructure evolution of as-cast and extruded WE43 magnesium alloy. Metals 2020;10(4):429.

[74] Chen Q, Lin J, Shu D, Hu C, Zhao Z, Kang F, et al. Microstructure development, mechanical properties and formability of Mg–Zn–Y–Zr magnesium alloy. Mater Sci Eng, A 2012;554:129–41.

[75] Stanford N, Sotoudeh K, Bate PS. Deformation mechanisms and plastic anisotropy in magnesium alloy AZ31. Acta Mater 2011;59(12):4866–74.

[76] Vagarali SS, Langdon TG. Deformation mechanisms in hcp metals at elevated temperatures—I. Creep behavior of magnesium. Acta Metall 1981;29(12):1969–82.

[77] Yoshinaga H, Horiuchi R. Deformation mechanisms in magnesium single crystals compressed in the direction parallel to hexagonal axis. Trans Jpn Inst Met 1963;4(1):1–8.

[78] Wang Y, Huang Y, Meng X, Wan L, Feng J. Microstructural evolution and mechanical properties of MgZnYZr alloy during friction stir processing. J Alloys Compd 2017;696:875–83.

[79] Ma ZY, Feng AH, Chen DL, Shen J. Recent advances in friction stir welding/processing of aluminum alloys: microstructural evolution and mechanical properties. Crit Rev Solid State Mater Sci 2018;43(4):269–333.

[80] Patel V, Li W, Vairis A, Badheka V. Recent development in friction stir processing as a solid-state grain refinement technique: microstructural evolution and property enhancement. Crit Rev Solid State Mater Sci 2019;44(5):378–426.

[81] McCafferty E. Introduction to corrosion science. Springer Science & Business Media; 2010.

[82] Hamu GB, Eliezer D, Wagner L. The relation between severe plastic deformation microstructure and corrosion behavior of AZ31 magnesium alloy. J Alloys Compd 2009;468(1–2):222–9.

[83] Silva CL, Oliveira AC, Costa CG, Figueiredo RB, de Fátima Leite M, Pereira MM, et al. Effect of severe plastic deformation on the biocompatibility and corrosion rate of pure magnesium. J Mater Sci 2017;52(10):5992–6003.

[84] Kutniy KV, Papirov II, Tikhonovsky MA, Pikalov AI, Sivtzov SV, Pirozhenko LA, et al. Influence of grain size on mechanical and corrosion properties of magnesium alloy for medical implants. Mater Werkst Entwickl Fert Prüf Eig Anwendungen Tech Werkst. 2009;40(4):242–6.

[85] Jiang J, Aibin MA, Saito N, Zhixin S, Dan S, Lu Fumin, et al. Improving corrosion resistance of RE-containing magnesium alloy ZE41A through ECAP. J Rare Earths 2009;27(5):848–52.

[86] Pu Z, Yang S, Song G-L, Dillon Jr OW, Puleo DA, Jawahir IS. Ultrafine-grained surface layer on Mg–Al–Zn alloy produced by cryogenic burnishing for enhanced corrosion resistance. Scripta Mater 2011;65(6):520–3.

[87] Ahmadkhaniha D, Fedel M, Sohi MH, Deflorian F. Corrosion behavior of severely plastic deformed magnesium based alloys: a review. Surf Eng Appl Electrochem 2017;53(5):439–48.

[88] Miyamoto H. Corrosion of ultrafine grained materials by severe plastic deformation, an overview. Mater Trans 2016;57(5):559–72.

[89] Son I-J, Nakano H, Oue S, Kobayashi S, Fukushima H, Horita Z. Effect of annealing on the pitting corrosion resistance of anodized aluminum-magnesium alloy processed by severe plastic deformation. Mater Trans 2008;49(11):2656–63.

[90] Abdulstaar M, Mhaede M, Wollmann M, Wagner L. Investigating the effects of bulk and surface severe plastic deformation on the fatigue, corrosion behaviour and corrosion fatigue of AA5083. Surf Coating Technol 2014;254:244–51.

[91] Liu Z, Bai S, Zhou X, Gu Y. On strain-induced dissolution of $þeta$′ and $þeta$ particles in Al–Cu binary alloy during equal channel angular pressing. Mater Sci Eng, A 2011;528(6):2217–22.

[92] Huang W, Liu Z, Xia L, Xia P, Zeng S. Severe plastic deformation-induced dissolution of $þeta$" particles in Al–Cu binary alloy and subsequent nature aging behavior. Mater Sci Eng, A 2012;556:801–6.

[93] Liu Z, Chen X, Han X, Gu Y. The dissolution behavior of $þeta$′ phase in Al–Cu binary alloy during equal channel angular pressing and multi-axial compression. Mater Sci Eng, A 2010;527(16–17):4300–5.

[94] Hou L, Wei Y, Shu X, Xu B. Nanocrystalline structure of magnesium alloys subjected to high energy shot peening. J Alloys Compd 2010;492(1–2):347–50.

[95] Veys-Renaux D, Chahboun N, Rocca E. Anodizing of multiphase aluminium alloys in sulfuric acid: in-situ electrochemical behaviour and oxide properties. Electrochim Acta 2016;211:1056–65.

[96] Mehdizade M, Soltanieh M, Eivani AR. Investigation of anodizing time and pulse current modes on the corrosion behavior of nanostructured anodic layer in commercial pure aluminum. :1–29.